minerals

MDPI

Article

Invisible Gold Paragenesis and Geochemistry in Pyrite from Orogenic and Sediment-Hosted Gold Deposits

Ross R. Large [1,*] and Valeriy V. Maslennikov [2]

[1] Australian Research Council Hub for Transforming the Mining Value Chain, Centre for Ore Deposits and Earth Science, University of Tasmania, Hobart 7005, Australia
[2] Institute of Mineralogy, Russian Academy of Science, Miass 456300, Russia; maslennikov@mineralogy.ru
* Correspondence: ross.large@utas.edu.au

Received: 13 February 2020; Accepted: 27 March 2020; Published: 9 April 2020

Abstract: LA-ICPMS analysis of pyrite in ten gold deposits is used to determine the precise siting of invisible gold within pyrite, and thus the timing of gold introduction relative to the growth of pyrite and related orogenic events. A spectrum of invisible gold relationships in pyrite has been observed which suggests that, relative to orogenic pyrite growth, gold introduction in some deposits is early at the start of pyrite growth; in other deposits, it is late toward the end of pyrite growth and in a third case, it may be introduced at the intermediate stage of orogenic pyrite growth. In addition, we report a distinct chemical association of invisible gold in pyrite in the deposits studied. For example, in the Gold Quarry (Carlin type), Mt Olympus, Macraes and Konkera, the invisible gold is principally related to the arsenic content of pyrite. In contrast, in Kumtor and Geita Hill, the invisible gold is principally related to the tellurium content of pyrite. Other deposits (Golden Mile, Bendigo, Spanish Mountain, Witwatersrand Carbon Leader Reef (CLR)) exhibit both the Au-As and Au-Te association in pyrite. Some deposits of the Au-As association have late orogenic Au-As-rich rims on pyrite, which substantially increase the value of the ore. In contrast, deposits of the Au-Te association are not known to have Au-rich rims on pyrite but contain nano- to micro-inclusions of Au-Ag-(Pb-Bi) tellurides.

Keywords: invisible gold; refractory gold; arsenic; tellurium; orogenic gold; Witwatersrand gold; Carlin deposits; LA-ICPMS; laser mapping

1. Introduction

Understanding the mineralogical siting of gold in ore deposits is an important aspect of ore genesis studies and geometallurgical research to increase the recovery of gold [1]. As more of the near-surface high-grade gold deposits are mined out across the globe, large low-grade (<2 g/t Au) deposits are the likely resources for the future. In most of these low-grade deposits, not all the gold is present as native gold grains and thus free milling, rather, most is present as invisible gold in sulfides particularly pyrite and arsenopyrite. The term invisible gold includes (1) nonstructural submicron scale particles (0.1 to 0.01 microns) and nanoscale (~1 to 10 nm) particles, and (2) structurally bound, solid solution or isomorphic states. Because invisible gold is difficult to separate and concentrate from the ores, it has become known as refractory gold. Refractory gold ores are generally far more expensive to process than free gold ores.

With the advent of new analytical technologies over the last 20 years, we are learning a lot more about refractory gold [2–8]. This research into refractory gold was spurred on by the discovery of the Carlin deposits in Nevada, which, in the primary zone, contain close to 100% invisible gold. Initial research indicated that invisible Au was preferentially concentrated in pyrite with high levels of solid

solution As, known as arsenian pyrite [9,10]. Arsenic can substitute into either the Fe site or the S site in pyrite and a maximum of 8%–11% As has been reported [11–13]. The position of ionic gold in the structure of pyrite is still not clear, although it is assumed that ionic gold Au^{+} substitutes for iron, entering distorted octahedral sites, whereas As substitutes for S in the tetrahedral sites [8]. Both surface speciation, and distortion-expansion of the pyrite lattice by incorporation of As are considered to be key processes in Au accumulation by arsenian pyrite [8,14].

A landmark publication [4] defined a relationship between the amount of invisible solid solution gold in pyrite and its arsenic content, using a database of analyses of pyrite from several Carlin and epithermal deposits. This maximum limit of invisible gold, from pyrite formed in the temperature range of 150 to 250 °C, is approximately 100 ppm Au for 2000 ppm As, and 1000 ppm Au for 2% As, and has become known as the saturation line for Au in arsenian pyrite (Figure 1; [4]). Gold analyses of pyrite that plot above the saturation line indicate free gold as nano- to micro- inclusions in pyrite. More recent research [5] has shown that the gold saturation line is most probably controlled by a number of factors, possibly including the crystal chemistry of pyrite and fluid/rock interactions and therefore different positions of the gold saturation line may need to be defined for each gold deposit type.

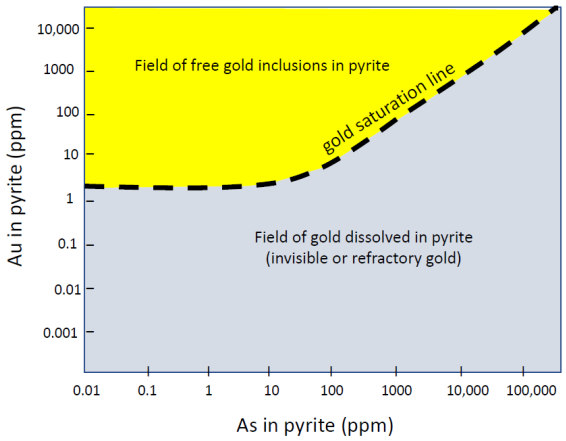

Figure 1. Au-As association in pyrite [4]. Data plotting below the gold saturation line (grey area) represents invisible gold dissolved in pyrite. Above the line (yellow area) gold is present as nano- to micro-gold inclusions in pyrite.

Second to As is the common association of Te with Au in many orogenic and epithermal gold deposits [15–18]. Well-known gold deposits with associated gold-silver tellurides are the Golden Mile deposit in Kalgoorlie, Western Australia; Cripple Creek, Colorado; Emperor, Fiji and Sandaowanzi, China [19]. Calaverite, krennerite and sylvanite are the most common Au-Ag tellurides with the formulae of $Au_{1-x}Ag_xTe_2$ [15]. Due to their common fine grain size and difficulties in recovery, Au tellurides in pyritic ores are considered refractory.

This study follows on from previous studies [20] that introduced the application of the laser ablation inductively coupled mass spectrometer (LA-ICPMS) analytical tool to the study of invisible gold in pyrite, using both spot analyses and laser mapping. Here, we have extended our research to include LA-ICPMS analytical data on pyrite in eleven orogenic and sediment-hosted gold deposits summarised in Table 1. This research was part of an industry funded AMIRA International project P1041. The emphasis here is on the timing of gold with respect to the orogenic hydrothermal growth of pyrite in each deposit, and other trace elements or pathfinders associated with invisible gold enrichment. We show that the technique of geochemical laser mapping of pyrite enables the determination of whether the main gold event was pre-orogenic, syn-orogenic or post orogenic. This study also highlights the common association of gold and tellurium in many orogenic deposits and suggests that a Au-Te association may be just as common as the Au-As association in pyritic sediment-hosted orogenic deposits.

Table 1. Some features of the Au deposits in this study.

Deposit	Country	Host Rocks	Number of Pyrites Analysed	Quartz Veins?	Free or Invisible Au in Pyrite	Metamorphic Grade	Au Association	Other Au Related Elements	Au-as Rims on Pyrite?	Au in Internal Pyrite?	Interpred Timing of Main Au Event(s)
Carlin (Gold Quarry)	USA	black mudstone	139	no	invisible Au	sub-greenschist	As-Au	As, Sb, W, Hg, Tl	Yes	no	short pulse latest orogenic (py2)
Macraes	New Zealand	schist	67	minor veinlets	Mainly free	upper greenschist	As-Au	Ni, W, Ti	No	throughout internal zones	syn-orogenic (py1 and py3)
Mt Olympus	Australia	black shale	115	no	both	greenschist	As-Au	Cu, Hg, Tl, Sb	rarely	one internal zone with Au	short pulse syn-orogenic (py2)
Konkera	Burkina faso	volcaniclastics	644	no	both	greenschist	As-Au	Ni	No	internal py2	early orogenic
Bendigo	Australia	shale, siltstone	231	saddle reefs	mainly free	lower greenschist	As-Au (-Te)	Ni	common	diagenetic cores have Au	pre-orogenic & latest orogenic (py1 and py3)
Sukhoi Log	Russia	black siltstone	264	minor veinlets	both	lower greenschist	As-Au (-Te)	Ni, Cu, Sb	No	Au in pyrite core & internal zones	pre-orogenic & syn-orogenic (py1 and py3/4)
Witwatersrand CLR	South Africa	conglomerate	958	no	both	lower greenschist	As-Te-Au	U, Ag, Co, Ni, Sb, Pd, Bi, Hg	Yes	Au in fractures in pyrite	pre-orogenic and syn-orogenic (py1 and Py2)
Golden Mile	Australia	dolerite	35	yes	both	lower greenschist	As-Te-Au	Ag, Cu, Sb	No	no data	no data
Spanish Mountain	Canada	black shale	28	no	both	lower greenschist	As-Te-Au	Ag, Ni, Pb	No	Au in pyrite core	pre-orogenic (py1)
Kumtor	Kyrgyzstan	black shale	180	no	both	lower greenschist	Te-Au	Co, Ni, Ag, Sb, Pb, Bi, As	No	Au in fractures in pyrite	pre-orogenic and post-orogenic (py1 and py3)
Geita Hill	Tanzania	BIF and chert	105	no	both	greenschist	Te-Au	Ag, Bi, Pb, Sb, Cu	No	Au with fine magnetite in pyrite core	? py2 replacing magnetite in BIF chert layers

It should be noted that this study is based on a limited number of samples from one lens of each deposit and may not be representative of the whole deposit. Sample numbers for each deposit vary from six to over 50, and the number of LA-ICPMS pyrite analyses from 28 at Spanish Mountain to 958 for the Witwatersrand CLR (Table 1).

2. Analytical Methods

The LA-ICPMS methods employed here are the same as those for our previous pyrite studies and the reader is referred to these papers [20,21] for more details. A brief summary follows. The instrumentation used in this study includes a New Wave 213 nm solid-state laser microprobe coupled to an Agilent 4500 quadrupole ICPMS housed at the CODES LA-ICPMS analytical facility, University of Tasmania. The laser microprobe was equipped with an in-house small volume (~2.5 cm^3) ablation cell characterised by <1 s response time and <2 s wash-out time. Ablation was performed in an atmosphere of pure He (0.7 L/min). The He gas carrying the ablated aerosol was mixed with Ar (1.23 L/min) immediately after the ablation cell and the mix is passed through a pulse homogenising device prior to direct introduction into the torch. The ICPMS was optimised daily to maximise sensitivity on mid- to high-mass isotopes (in the range 130–240 a.m.u.). Each analysis was performed in the time-resolved mode, which involves sequential peak hopping through the mass spectrum.

For this study, the quantitative analyses were performed by ablating spots ranging in size from 25 to 40 microns. The laser repetition rate was typically 5 HZ and laser beam energy at the sample was maintained between 4 and 5 J/cm^2. The analysis time for each sample was 100 s, comprising a 30 s measurement of background (laser off) and a 70 s analysis with laser on. The acquisition time for most masses was set to 0.02 s. However, major silicate elements (Mg, Al, Si, Ca) and S were measured for 0.005 s, trace silicate elements (Zr, Ba, La, Th, U) and Cd for 0.01 s, Se, Mo and Ag for 0.1 s, Te for 0.2 s, and Au for 0.4 s, with a total sweep time of ~1.5 s. Data reduction was undertaken according to standard methods [19], using Fe as the internal standard. An in-house Li-borate-fused glass of a pyrite/sphalerite mixture [22] was used as the primary calibration standard. The standard was analysed twice at every one and a half hour to account for the instrument drift, with a 100 μm beam and at 10 Hz.

Mapping of pyrite was performed by ablating sets of parallel lines in a grid across the samples. Depending on the sample size, lines were ablated with a beam size of 15 or 25 μm. The spacing between the lines was kept constant at the same size as the laser beam. The lines were ablated with a repetition rate of 10 Hz, and rastering at 15 or 25 μm/s, depending on the spot size. Thus, every position on the sample was ablated 10 times and its composition contributed to 10 consecutive pixels on the image, resulting in an unprocessed effective resolution matching the beam size. A set of 20 elements was analysed, with the acquisition time for most masses set to 0.002 s. However, to improve their detection limits, Se was measured for 0.004 s and Ag, Te and Au for 0.04 s. The total sweep time was ~0.2 s. To allow for cell wash out, a delay of 13 s was used after each line. Background levels and the primary sulfide standard [19] were measured before and after each image.

Image processing was as follows: (1) ICPMS sensitivity drift was corrected for each element individually, based on the standard measurements before and after image acquisition; (2) a median filter was applied to remove spikes originating from counting statistics; (3) the average background for each element was subtracted from the filtered counts; (4) for each element, background-corrected counts that were below the standard deviation on the average background were assigned the standard deviation value; (5) images were then produced for each element using a logarithmic colour scale.

3. Siting of Invisible Gold in Pyritic Ores and Its Significance

Hydrothermal pyrite is commonly zoned, with several generations of pyrite precipitated over the previous generation (e.g., Figure 2; [23,24]). It is common to find at least three generations (py1, py2, py3), but up to six generations are known from some deposits (e.g., Sukhoi Log, Russia, [23]). It seems that pyrite preferentially precipitates on pyrite, rather than starting a new nucleation point.

Thus, each Fe- and S-saturated fluid event is represented by a new and commonly distinct overgrowth of pyrite (Figure 2). The number of pyrite-precipitating fluid events associated within a deposit can be documented by etching and studying pyrite aggregates in the ores [25,26].

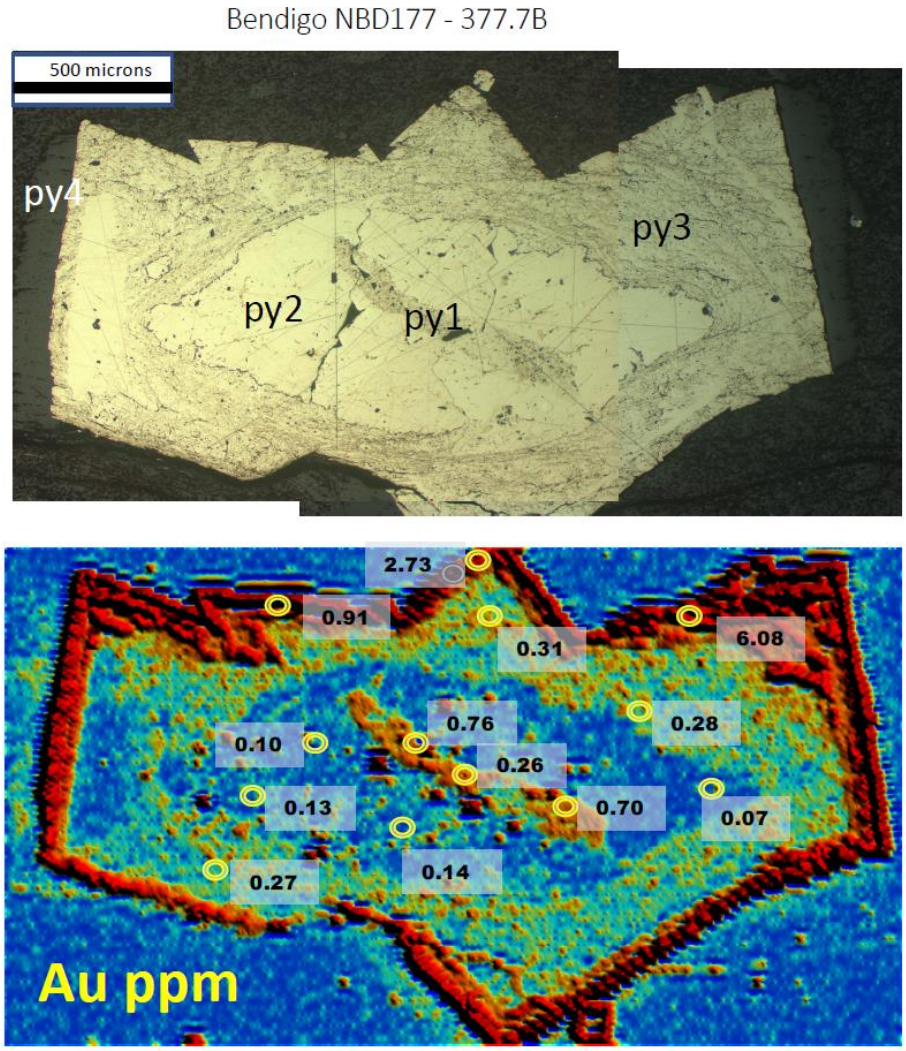

Figure 2. Pyrite aggregate from the pyritic halo of a Bendigo quartz-Au lode [27]. Top panel (**A**), photomicrograph reflected light of the pyrite aggregate showing the pyrite zones, py1 core, py2, py3 and py4 rim. Bottom panel (**B**), LA-ICPMS map of Au; colours from blue, green, yellow, orange and red represent increasing gold content on a log scale. Numbers in grey oblongs are spot analyses in ppm Au, by LA-ICPMS.

In combination with laser mapping, it has been possible to determine the timing of the introduction of invisible gold into the pyrite paragenesis (i.e., py1, py2, py3, etc.) and define other path finder trace elements that were introduced into the pyrite at the same time as the Au event.

For ten of the eleven deposits considered in this study, we have provided laser trace element maps of gold and key elements in pyrite (Figures 3–9) and discuss the siting of invisible and native gold for each case. The studies are grouped below according to the main gold stage with respect to pyrite growth.

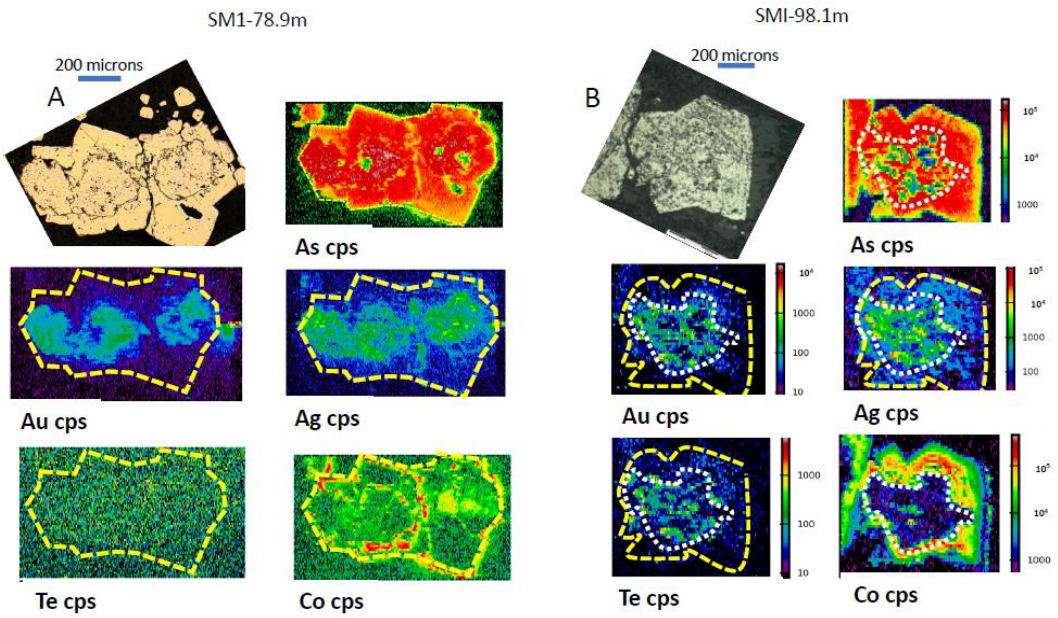

Figure 3. Two contrasting laser ablation inductively coupled mass spectrometer (LA-ICPMS) images in counts per second (cps) of pyrite from the Spanish Mountain deposit. (**A**) Au, As and Ag concentrated in the core (py1), and no Te. (**B**) Au, Te and Ag in the core (py1), with Co, As in the euhedral rim with no Au. Cold colours (blue, green) represent low concentrations; hot colours (yellow, orange, red) represent high concentrations.

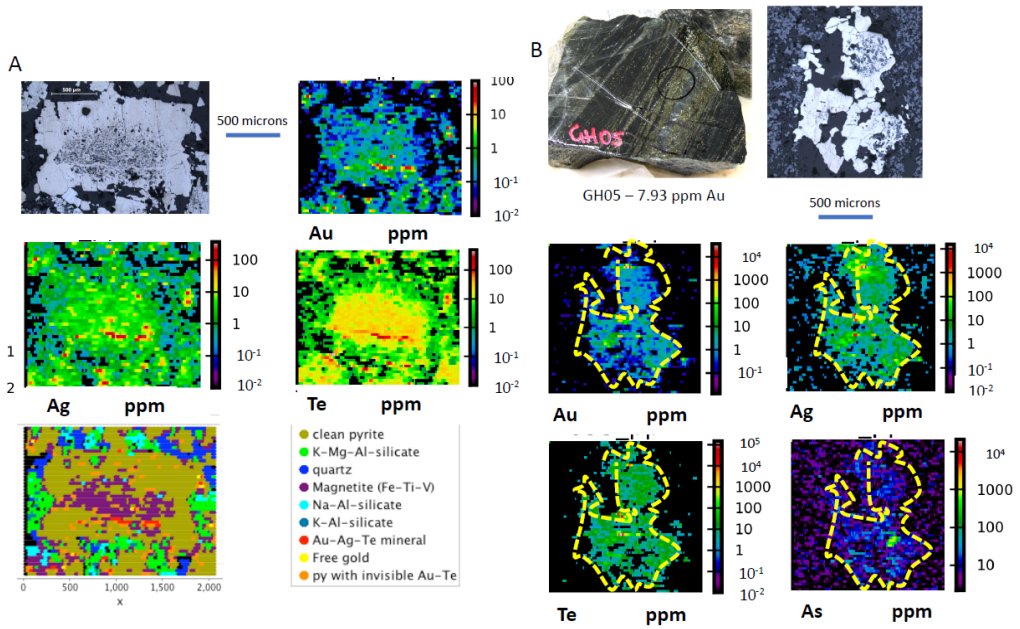

Figure 4. LA-ICPMS maps of pyrite in ppm from Geita Hill. (**A**) Large (2 mm across) euhedral pyrite with fine magnetite inclusions in the core. Laser maps show Au, Ag and Te concentrated in the pyrite core with magnetite inclusions. Red spots on the images represent extra high concentrations of coincident Au, Ag and Te caused by micro-inclusions of Au-Ag tellurides. The bottom left image is a reconstructed mineralogy map based on the laser geochemistry, with the legend to the right. (**B**) Irregular anhedral pyrite aggregate in a silica-rich band in BIF. Micro-inclusion of magnetite in the pyrite represent relicts of sulfidised magnetite. Invisible Au, Ag and Te are throughout the pyrite aggregate, but very little As.

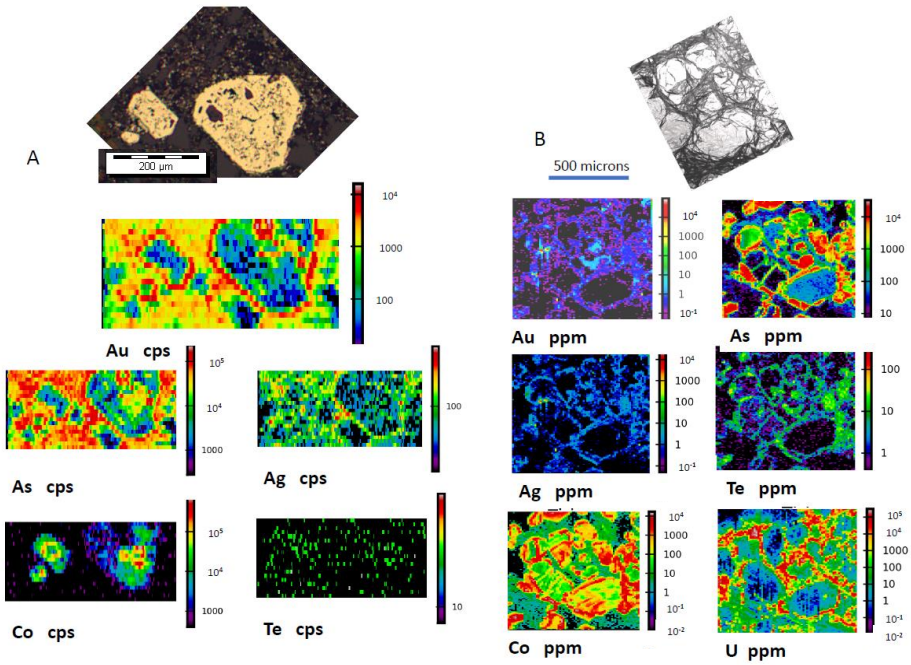

Figure 5. (**A**) LA-ICPMS map of pyrite in cps from Carlin deposit Gold Quarry showing the characteristic Au-As rim on pyrite and Co-rich core to the pyrite. (**B**) LA-ICPMS map in ppm of a cluster of detrital pyrites from the Witwatersrand Carbon Leader Reef. The hydrothermal rims on detrital pyrites are enriched in As, Ag, Co, Te, Au and U.

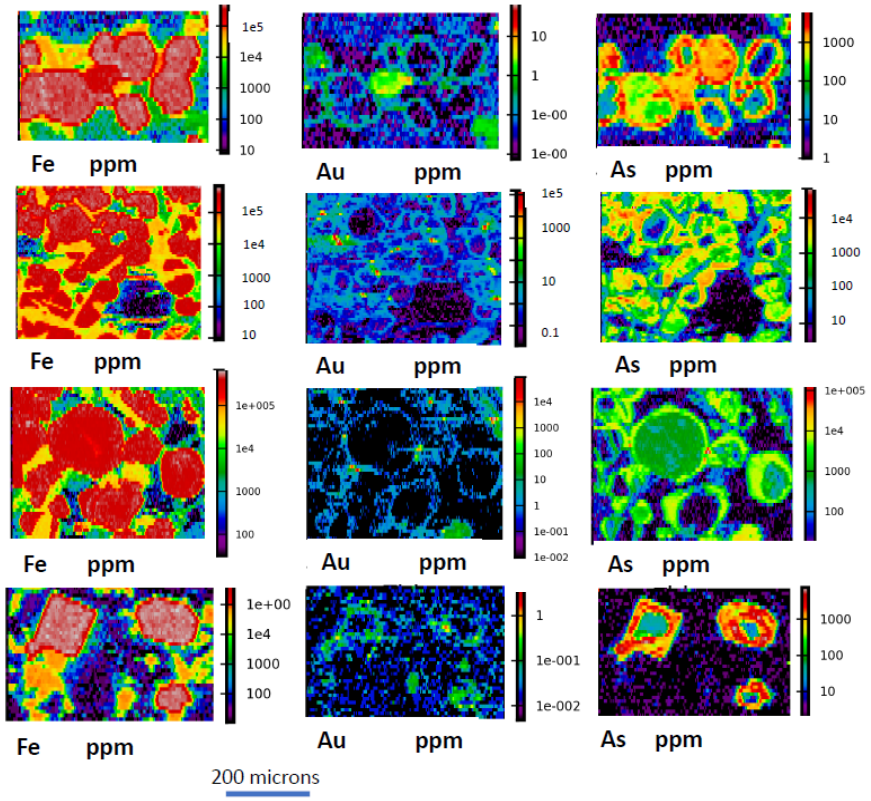

Figure 6. Four examples of pyrite rims on pyrite in the Carbon Leader Reef (CLR) distinctly outlined by elevated As and Au. All maps in ppm. High Fe ppm (red-white) show the pyrite. The red-orange-yellow spots on the gold images indicate micro-particles of free gold on the invisible gold bearing arsenian pyrite rims.

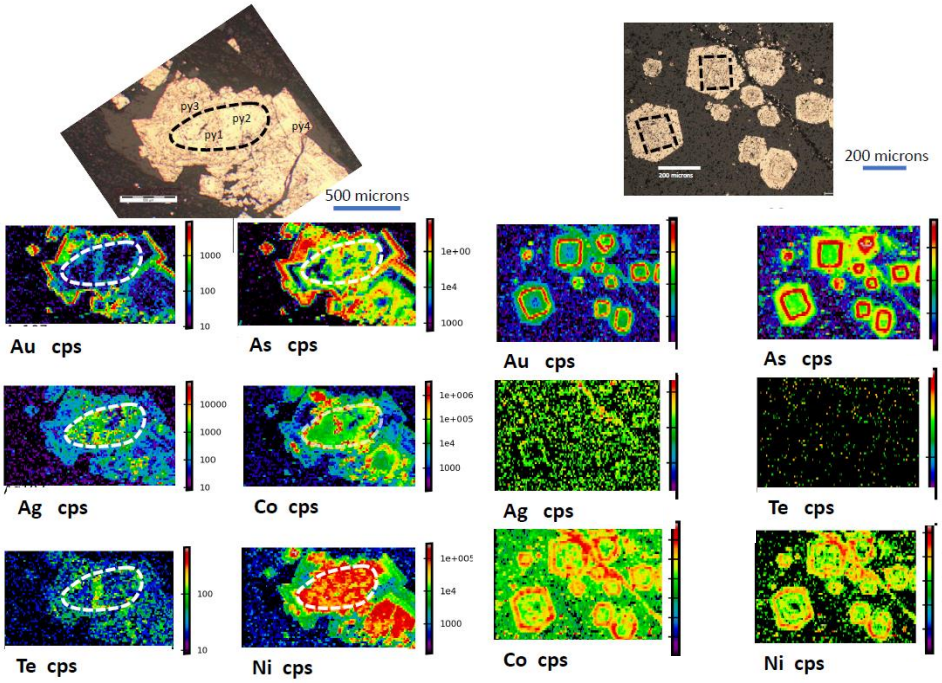

Figure 7. (**A**) LA-ICPMS maps of pyrite aggregate from disseminated pyrite halo, Bendigo quartz reefs [27]. Note the Ni-rich nodular core (py1 and py2) and the Au-As-rich rim (see also Figure 2). (**B**) LA-ICPMS maps of pyrite euhedra from the Mt Olympus deposit. Au and As enrichment (red) is present as an internal band, surrounded by a Co-Ni-bearing rim.

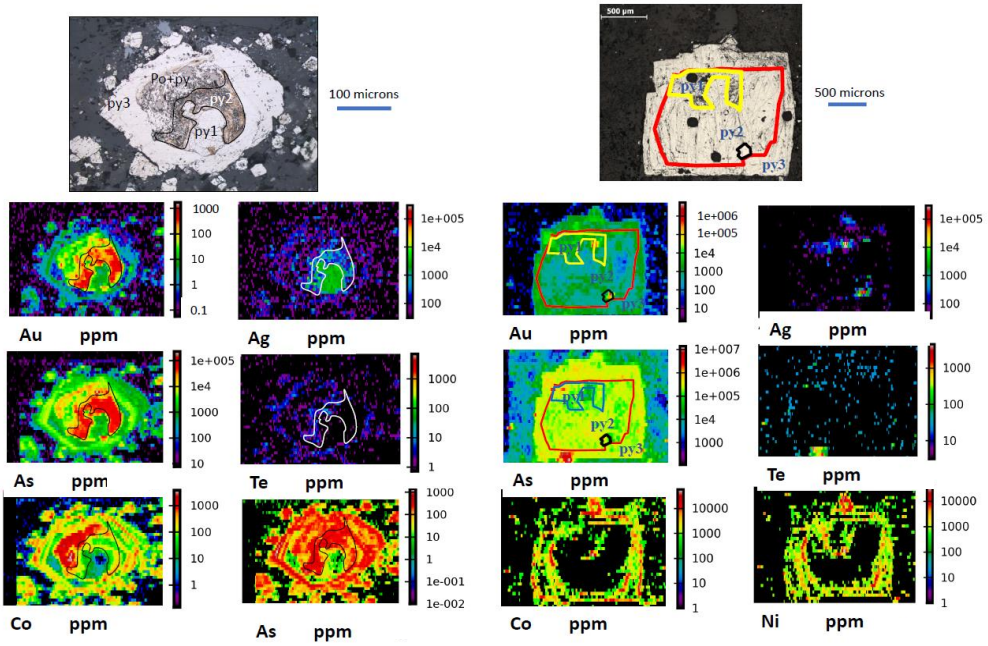

Figure 8. (**A**) LA-ICPMS maps in ppm of complex pyrite aggregate from the Konkera Deposit. Py2 carries the maximum Au and As, with an outer zone enriched in Ni, Co and As, but lesser Au. (**B**) A typical pyrite from Macraes Deposit with LA-ICPMS maps in cps. Three pyrite zones py1, py2, py3 all carry significant Au, As but no Te or Ag. Nickel and Co concentrated in the outermost py3. Free Au micro-particles are indicated by red spots on the Au map.

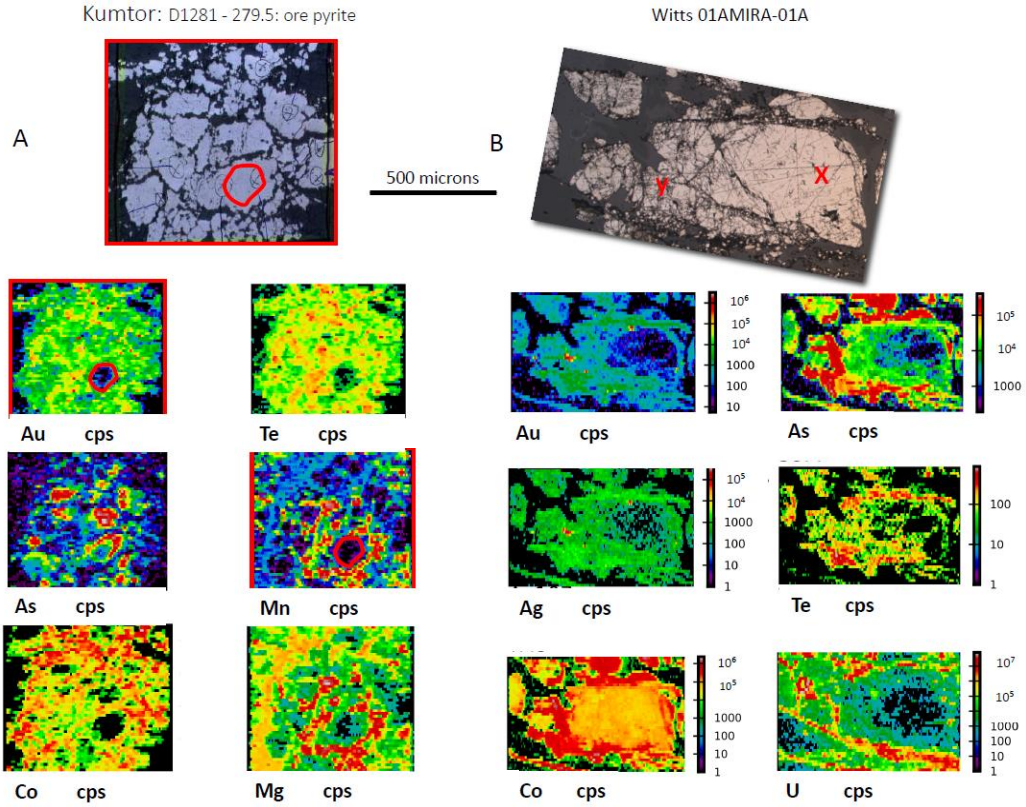

Figure 9. Gold in fractured pyrite. (**A**) LA-ICPMS maps in cps of fractured pyrite from the Kumtor deposit, Kyrgyzstan. Invisible Au-Te is indicated by the green and yellow, whereas orange and red indicate locations of nano- to micro-inclusions of Au tellurides. Arsenic is rimming some pyrite fragments. Mn and Mg suggest an initial core of Mn-carbonate was replaced by pyrite. (**B**) Fractured and brecciated pyrite from the Witwatersrand CLR. LA-ICPMS maps in cps. The intensely brecciated pyrite shows elevated invisible Au, As, Ag, Te, Co and U, suggesting that these elements were added to the pyrite during a later hydrothermal event. Corresponding red spots on the Au and Ag maps indicate the position of free electrum. Red X marks unfractured pyrite and red Y fractured pyrite.

3.1. Gold Predominantly in the Core of Pyrite (py1)

Two deposits from the eleven studied show invisible gold concentrated in the core of pyrite aggregates in deformed sedimentary rocks—Spanish Mountain in British Columbia and Geita Hill in Tanzania (Table 1). Spanish Mountain is a gold bearing disseminated pyrite deposit hosted in Triassic black shales and greywackes at the base of the Quesnel Trough, a continental margin sequence in central British Columbia [27]. Drilling has defined a resource of 67 Mt at 0.8 g/t Au in a zone of disseminated pyrite, carbonate alteration and minor quartz veining within a strongly deformed sequence of phyllites and meta-volcaniclastics. Gold is present in the pyritic black slates and phyllites and in associated quartz veins. We have investigated pyrite textures and geochemistry from one drill hole passing through the main mineralised zone [20].

Results from the laser mapping of two Spanish Mountain pyrites are shown in Figure 3. In the first case (Figure 3A), gold is uniformly distributed through the core of the pyrite (py1) and is associated with elevated As and Ag. Laser spot analyses indicate the core averages 9.6 ppm Au, 13,000 ppm As, 20 ppm Ag and 2.0 ppm Te, with a Ni/Co ratio of 100. The outer euhedral pyrite overgrowth has a completely different trace element chemistry to the core averaging 0.17 ppm Au, 4360 ppm As, 9.5 ppm Ag and 1.9 ppm Te, with a Ni/Co ratio of 2 compared to the core pyrite. The rounded shape of the pyrite core, its high Ni/Co ratio and Ag/Au > 10 suggest that it maybe original diagenetic pyrite in the black shale host rocks [20,28]. On the other hand, the euhedral shape of the pyrite overgrowth

and its low Ni/Co ratio indicate that it is likely metamorphic and syn-orogenic. Based on this pyrite, and other pyrite from this and adjacent samples, the main gold event is pre-orogenic, and related to diagenetic processes in the black shale host rocks. The later orogenic fluid event that produced the overgrowth py2 contains elevated As but little Au and appears to be unrelated to the main gold event at Spanish Mountain.

Laser mapping of a second type of pyrite aggregate at Spanish Mountain (Figure 3B) indicates invisible Au is present in the core of the pyrite as before, with the euhedral syn-orogenic pyrite overgrowth lacking significant gold. However, in contrast to the previous example, the gold distribution in the core is very irregular from <1 to over 100 ppm Au and shows a strong spatial relationship to spikes in Te, Ag (Figure 3B) and Bi, Pb. This pattern of Au spikes in the core (py1) with enriched Te, Ag, Bi, Pb is typical of micro inclusions of Au-Ag-Pb-Bi tellurides [23]. The later generation of euhedral overgrowth pyrite (py2) is generally lacking in most trace elements except Co, As and Ni, with a Ni/Co ratio of 3. The core pyrite has a Ni/Co ratio of 750, with an irregular anhedral, possibly corroded outline and maybe an original diagenetic pyrite as in the previous example (Figure 3A). The micro inclusions of Au-Ag tellurides may have been formed during diagenesis, and if this is the case, then the gold is likely to be pre-orogenic.

Two examples of invisible gold in pyrite from the Geita Hill orogenic deposit, Tanzania, are shown in Figure 4A,B. Here, the host rock is banded iron formation, where the pyrite occurs in bands over printing magnetite grains (Figure 4A). Pyrite grains are subhedral and contain abundant inclusions of magnetite residuum after replacement by pyrite. In Figure 4A, a large pyrite subhedra has invisible Au concentrated in the core spatially associated with an increase in the density of magnetite inclusions. Gold, Te and Ag concentration in the pyrite appear to decrease from core to rim of the pyrite. The coincidence of red spikes in the Au, Te and Ag images indicates some micro-inclusions of Au-Ag tellurides, otherwise SEM scanning suggests that most of the gold appears to be associated with Te and Ag in solid solution or as invisible nano-inclusions less than 5 nm in size in the pyrite. The intimate association of Au with relics of magnetite suggests that sulfidation of magnetite in certain BIF layers was the key process in the precipitation of gold (c.f. [29]). Arsenic is uniformly low (<50 ppm) in all pyrite from these Geita Hill samples. Such low levels of As is rare in most orogenic gold deposits. The relationship of the Au-Ag telluride event to orogenesis is not clear from these samples. The primary conclusion is that Au, Ag and Te were emplaced during sulfidation of magnetite in the BIF host rocks.

3.2. Gold Concentrated on the Rim of Pyrite

The classic case of invisible gold on pyrite rims is found in Carlin deposits [30,31]. An example is shown in Figure 5A, but better examples are found in [32]. The Au-As rims vary in thickness from a few microns to rarely over 10 microns. Our LA-ICPMS data indicates that Au content in the rims can vary from 5 to 5000 ppm and As from 1000 to 50,000 ppm, with mean Ni/Co ~15 and mean Ag/Au ~0.01 (based on pyrite from Gold Quarry and Gold Strike). The pyrite cores commonly contain negligible Au and, depending on the nature of the host rock, are commonly diagenetic pyrite enriched in Co and Ni compared with the Au-As rim. As seen in Figure 5A, Te is commonly negligible in both the core and rim. There are several other examples of Carli- type deposits, especially in southern China, that show Au-As enrichment on pyrite rims (e.g., Shuyindong deposit in SW China, [33]).

A second example of invisible gold-bearing rims on pyrite is present in the giant Witwatersrand Carbon Leader Reef (CLR) deposit in South Africa [21]. A major controversary has existed for more than 100 years over the origin of the Witwatersrand gold deposits, with the two major competing theories claiming either a detrital origin [34] or a hydrothermal origin [32] for the gold. However, recent studies of the pyrite in the conglomerate lenses of the CLR have confirmed that both theories are likely to be correct with syn-sedimentary gold deposition being followed much later by a hydrothermal (syn-orogenic) gold event [21]. The principal evidence for the hydrothermal event is the invisible gold rims on rounded detrital pyrite in the high-grade layers of the conglomerates, particularly the CLR. Figure 5B shows clusters of rounded to sub-rounded pyrite grains from 50 microns to 2 mm across,

each with an arsenic-rich rim that is also enriched in Au, Te, Ag, Co and U compared with the pyrite cores. The rims are commonly 20–30 microns thick, with a very consistent geochemistry (high Au, As, Te, Ag, Co, Ni, Pb, Sb and U).

Free gold grains are present in some CLR pyrite rims, as shown by the laser mapping, as bright red and yellow spots in Figures 5B and 6. The mean invisible gold content of the rims mapped in Figure 6 varies from 0.2 to 2 ppm, and As content from 1000 to 8000 ppm. Rims with the highest As content (Figure 6) have a higher content of free gold micro-grains. Lead isotope ratios on the rims indicate they may have formed up to 600 million years after the detrital pyrite cores. [21,25]. In the detrital gold model [34] the pyrite rims on detrital pyrite cores are considered to be diagenetic in origin, and therefore do not support a major hydrothermal event that has introduced gold into the reefs. However, we argue that the uniform thickness and geochemistry of the rims, the high Co concentration and the presence of free gold micro-grains on the most As-rich rims throughout all samples studied from the CLR, supports a uniform hydrothermal event that introduced a significant amount of Au into the CLR.

A third example of invisible gold on pyrite rims is reported from the disseminated pyritic halo developed in sedimentary rocks surrounding the quartz vein gold reefs of the Bendigo deposit [24]. Pyrite aggregates in black shales adjacent to the free gold-bearing quartz lodes show a complex overgrowth history (Figures 2 and 7A). The small pyrite core (py1) is inclusion-rich and surrounded by an elongate nodule (py2) of likely late diagenetic origin. py3 with a metamorphic fabric, overgrows the nodule and is interpreted as mid to late orogenic. Finally, a euhedral rim (py4) is the last pyrite to form, during latest orogenesis. LA-ICPMS mapping (Figure 2) indicates minor Au (~0.7 ppm) in the py1 core, no gold in the diagenetic nodule, and gradually increasing gold through the metamorphic overgrowth (~0.2 to 0.4 ppm) reaching a maximum on the pyrite rim (1 to 6 ppm Au and 2800 to 8500 As). The Ag/Au = 19.4 and Ni/Co = 16.8 supports a diagenetic origin for py1, whereas Ag/Au = 0.7 and Ni/Co = 6 supports an orogenic origin for py4 the rim. Our interpretation of the pyrite aggregate in Figures 2 and 7A is that there were two gold events at Bendigo: firstly minor invisible gold was concentrated in the py1 cores during early sediment diagenesis and secondly during basin inversion the orogenic fluids became increasingly gold-rich, with maximum gold and arsenic introduction to form high-grade ores in the final phase of orogenesis. These LA-ICPMS mapping results support previous structural interpretations [35] that the main gold event was during fault lock-up at the end of the main orogenic phase.

Other examples of invisible gold rims on pyrite have recently been reported from epithermal Au deposits and distal disseminated hydrothermal-magmatic gold deposits [36].

3.3. Gold Concentrated in Internal Zones of Pyrite

Three case studies are discussed here: The Mount Olympus gold deposit in the Capricorn Orogen of Western Australia, the Konkera gold discovery in Burkina Faso, West Africa and the Macraes Flat gold deposit in New Zealand.

Mount Olympus was initially described as an orogenic gold deposit [37], but more recently considered to be a Carlin-type deposit formed during orogenesis at 1769 Ma [38]. The deposit has a total remaining resource of 15 million tonnes (Mt) at 2.2 g/t (Northern Star Resources Limited, 2015). Both strata-bound and fault-controlled mineralisation are present in Proterozoic shales and conglomerates. Evidence in favour of a Carlin-type origin ar; the trace element chemistry of the pyrites which closely resembles those of the Carlin deposits of Nevada, including rims that display solid solution gold accompanied by elevated As, Cu, Sb, Hg, and Tl, surrounding gold-poor cores. Although some pyrite exhibits thick diffuse rims of gold-rich arsenian pyrite ([38]; Figure 8), most other examples (Figure 7B) show internal gold-rich bands. The internal band shown in Figure 7B is ~10 microns thick, carrying ~70 ppm Au, 5% As and elevated Cu, Hg, Tl and Hg, very similar to the Carlin rims discussed earlier. In comparison, the pyrite core is very low in trace elements and the rims at Mount Olympus are gold poor, with only elevated Co (Ni/Co = 0.05). Our conclusion, based on the pyrite zonation and

geochemistry, is that Mt Olympus has features similar to Carlin-type deposits, but in this case, a later orogenic fluid flow event produced an outer rim on the pyrite with enriched Co but little gold.

Pyrites in the orogenic gold Konkera deposit in West Africa exhibit a very complex hydrothermal history (Figure 8A), with the best gold confined to internal zones in the pyrite aggregates. The deposit is a disseminated pyrite concentration in altered volcaniclastics and basalts on the western margin of the Boromo Greenstone belt in SW Burkina Faso. The global resource is 59 mt at 1.7 g/t Au [39]. It has been classified as a shear zone hosted late orogenic Au deposit [39,40]. Figure 8A is typical of the pyrite aggregates in the mineralised zone and indicates three generations of pyrite.

Py1 has an anhedral shape, commonly corroded by py2 and is enriched in Sb, Cu, Zn, Ag, Pb and Hg, but little gold. py2 is related to the main gold event carrying free gold grains and invisible gold from 10 to 3000 ppm Au, and As from 1% to 5.5%, plus elevated Ni from 30 to 700 ppm. Py3 formed after the main gold event being enriched in only Se, Co and Ni with very minor Au. In some examples, pyrrhotite is present between py2 and py3. Overall, the trace element zonation in pyrite aggregates is as follows [41]:

Core Hg, Te, Ag, Pb, Sb, Tl, Cu →	Au-As-Ni →	Ni, Se, Co Rim
py1	py2	py3

The trace element associations suggest py1 is related to a low-temperature volcanogenic fluid, whereas py2 and py3 are most likely higher temperature fluids, py3 being of orogenic origin. The main gold event (py2) appears to be pre- or early orogenic, whereas the main orogenic pyrite (py3) appears to carry little gold. Lead isotopes ratios suggest that py3 is ~100 to 200 million years after the py2 gold event [41].

Macraes is a 7 M oz. shear zone hosted deposit in the Mesozoic Otago Schist belt of greenschist facies [42–44]. Pyrite aggregates commonly show three distinct overgrowth pyrite generations [45]. In Figure 8B, all three euhedral pyrite generations are apparent, a small core or corroded py1, surround by py2 with a euhedral rim of py3. The laser mapping shows that all three pyrite generations contain invisible gold related to a high As content, but no Te or Ag. Free electrum grains are common at the boundaries of py1/py2 and py2/py3. Detailed study of many pyrite aggregates [46] indicates py1 is variably enriched in invisible Au (1 to 28 ppm), As (6000 to 20,000 ppm) plus W, Ni, Th and Ti. Py2 is As rich (700 to 10,000 ppm), with minor Au (0.3 to 5 ppm) but no other significant trace elements. Py3 is similar to py1, with Au from 1 to 30 ppm, As from 3000 to 15,000 ppm, plus elevated Ni, Co, Pb, Bi, Cu, Ti and W. All three generations have below-detection Te and very low Ag/Au ratio (<0.1), indicative of orogenic pyrite. In conclusion, gold mineralisation at Macraes was a protracted event, involving three episodes of Au-As fluid flow accompanying three separate orogenic pulses.

3.4. Gold Concentrated in Fractured Pyrite

The best examples of gold in fractured pyrite, studied by our group, are at the Kumtor Au deposit in Kyrgyzstan and the Witwatersrand CLR in South Africa (Figure 9). Kumtor is a strata-bound orogenic gold deposit hosted in deformed and sheared Neoproterozoic to Cambrian pyritic black shales with minor sandstones and limestones of the Middle Tien Shan belt, Central Asia [47,48]. Gold is hosted in pyrite as free gold, gold tellurides and invisible gold. Previous research [49] demonstrated that sedimentary pyrite nodules in the black shales contain high levels of Au, Ag, Pb and Te and most probably constitute the source for these metals in the orogenic deposit.

Orogenic pyrites in the Kumtor deposit vary from subhedral zoned varieties to fractured types, as shown in Figure 9A. Here, Au, Te, Ag and Co are distributed unevenly through the fractured pyrite. Red spikes in Au and Te indicate free micro-grains of Au tellurides. SEM studies suggest some of the gold-silver-bearing tellurides occur as nano-inclusions (2 to 150 nm) along pyrite grain boundaries. The original core of the pyrite is indicated by the Mn and Mg maps (Figure 9A), suggesting replacement of a carbonate crystal. The intensity of invisible Au and Te distribution or penetration into the fractured

pyrite possibly suggests that gold mineralisation accompanied fracturing of the pyrite as part of the late orogenic event. Based on several laser ICPMS maps of the ores and host rocks [46] the pyrite-gold paragenesis at Kumtor can be summarised as:

- Early diagenetic py1 enriched in Au, Te, Pb, Sb, Bi, Mo, As, Ag, V and U;
- Overgrowth late diagenetic to early metamorphic pyrite enriched in Co, Ni, As, and Se;
- Early orogenic pyrite enriched in Au, As, Te, Ag, Pb, and Sb;
- Late orogenic pyrite overgrowths and pyrite fracturing carry Co, Ni, W, Au, and Te. This late orogenic event introduced the maximum pulse of gold.

Earlier we described gold-enriched pyrite rims on detrital pyrite, which provided the evidence for a major hydrothermal (orogenic?) gold event superimposed on the Carbon Leader Reef (CLR). In Figure 9B, large fractured detrital pyrites in the CLR are enriched in Au, Ag, Te, Co and U again providing evidence for the late orogenic fluid gold event. The intensity of gold and other trace elements is directly related to the degree of fracturing of the pyrite. The relatively unfractured pyrite (point X, Figure 9B) toward the centre of the pyrite grain carries very low trace elements and presumably was not affected by the hydrothermal fluid. Fracturing and Au-As-Te-Ag-U concentration increase toward point Y, with free Au micro-grains present in the most intensely fractured areas. This is clear evidence for a fluid penetrating the pyrite along the fractures, and contributing Au, As, Te, Ag, Co and U as mineral nano-grains or by substitution into the pyrite structure. The complex set of elements added to the fractured pyrite is the same as those in the pyrite rims coating detrital pyrites elsewhere in the CLR (Figure 6, [21]).

4. Chemical Associations of Invisible Gold

4.1. Gold-Arsenic Association

Two of the eleven deposits discussed above show a strong association between Au and As (Gold Quarry and Mt Olympus). A further two show a strong association between Au and Te (Kumtor and Geita Hill). The remaining seven deposits show associations of Au with both As and Te. Figure 10A shows the Au-As association in pyrite from Gold Quarry and Mt Olympus. The Gold Quarry pyrite data sits immediately under the saturation line, which is expected because the line was originally defined on the basis of analytical data from Carlin deposits [4]. This relationship means that many of the pyrite rims from Gold Quarry carry the maximum amount of invisible gold possible for their given As content.

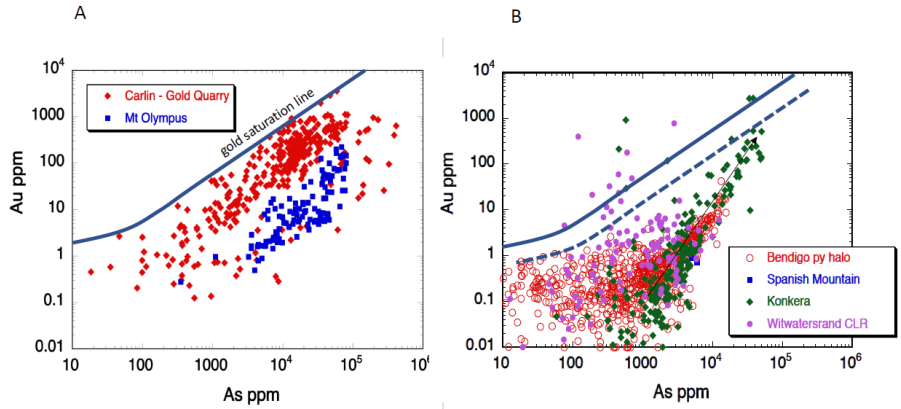

Figure 10. LA-ICPMS data plotted on the As-Au diagram for (**A**) Gold Quarry and Mt Olympus, (**B**) Bendigo pyrite halo, Spanish Mountain, Konkera and Witwatersrand CLR pyrite rims. The gold saturation line for the four deposits in panel (**B**), may be an order of magnitude lower (dashed line) than for Gold Quarry in panel (**A**) (solid line).

In contrast, the Mt Olympus pyrite data shows the pyrite has an order of magnitude less invisible gold than Gold Quarry. The pyrite from Konkera, Spanish Mountain and the pyritic halo at Bendigo (Figure 10B) also plot lower in the diagram similar to Mt Olympus, carrying much less invisible gold than Gold Quarry, except for a few analyses of py2 from Konkera with As > 2% and Au > 100 ppm. Much of the pyrite in the halo at Bendigo has As < 1000 ppm and Au < 1 ppm, but the Au and As increase on the pyrite rims with increasing proximity to the gold-quartz lodes [24]. Pyrite rims on the detrital pyrites in the Witwatersrand CLR, plot with the bulk of the other orogenic deposit data. However, there is a vertical trend of some data that plots above the gold saturation line (Figure 10B). These represent analyses of rims on detrital pyrite that include micro-grains of free gold (Figure 6).

The pyrite data in Figure 10B for the orogenic deposits and the CLR suggests the gold saturation line for these deposits may be considerably lower than for Carlin deposits, somewhere in the position of the dashed line in Figure 10B. Different positions of the gold saturation line for different ore types, have previously been investigated [5]. This is significant, as the ratio of free gold to invisible gold will increase for deposits with lower saturation lines. Factors controlling the hydrothermal transport and adsorption of gold on pyrite will likely affect the position of the gold saturation line in pyrite for any given deposit, particularly temperature, fO_2 and pH [14].

4.2. Gold-Tellurium Association

Pyrite in samples from Geita Hill, Kumtor and the Golden Mile (Fimiston) all show a strong positive relationship between Au and Te (Figure 11A). This is also clear from the laser maps (Figures 4 and 9A) where micro-grains of Au tellurides have been revealed within pyrite containing a high background of invisible Au and Te. Pyrite containing from 100 to 1000 ppm Te carries from 1 to 100 ppm Au. Most of the pyrite data (Figure 11A) is constrained within ratio boundaries of Au/Te = 1 to 0.01 equating to sylvanite with a composition from $AuAgTe_4$ to $Au_{0.1}Ag_{1.9}Te_4$ (Figure 11A). Recent research [46] has shown that the main tellurium bearing minerals at Geita Hill, in addition to sylvanite, are nagyagite [$Pb_3(Pb,Sb)_2S_6(Au,Te)_2$] and calaverite $AuTe_2$. Whereas Geita Hill and Kumtor show a weak negative correlation with As, the Golden Mile pyrites exhibit both a positive correlation between Au-Te and Au-As (Figure 11B). This dual association in the one sample set, even on a pyrite grain by grain basis in a single sample, is unique amongst the deposits studied here. All three deposits also show positive correlations between Au and Ag, Pb and Bi (Figure 11C–E). These patterns confirm that some or all of the gold is present in pyrite as a Au-Ag telluride or maybe perhaps a complex Au-Ag-Pb-Bi telluride. Whether the tellurides occur solely as an array of various sized micro- to nano-inclusions or as some complex solid solution in pyrite cannot be determined from our data. Structurally bound Te-bearing complexes, such as $Fe(SAs)\text{-}Au(HTe)^0$ or $Fe(SAs)\text{-}Au_2Te^0$, have been suggested to explain the high Au, As, and Te contents of pyrite [50,51]

Mean values of Au, As and Te in pyrite from the eleven deposits (plus Sukhoi Log; [26]) are listed in Table 2 and plotted in Figure 12A,B. These diagrams, particularly Figure 12B, display a spectrum of deposits from the As-Au end members (Carlin, Mt Olympus, Macraes) to the Te-Au end members (Geita Hill and Kumtor). In the middle of the spectrum are Bendigo, Spanish Mountain, Sukhoi Log, Konkera and the Witwatersrand CLR pyrite rims, which exhibit both the Au-As and Au-Te associations. The mean Golden Mile pyrite lies off the trend due to above average levels of both As and Te.

In terms of Au-Ag associations in pyrite (Figure 13), deposits exhibiting a Au-As association have a Ag/Au ratio varying from 0.01 to 1.0, whereas deposits with a Au-Te association have higher levels of Ag and a Ag/Au ratio of 1.0 to 10. This is due to the common link between Ag and Te forming Au-Ag tellurides in Geita Hill and Kumtor. Sedimentary pyrite has a much higher Ag/Au ratio varying up to 1000 and this turns out to be a useful criterion to assist in distinguishing disseminated sedimentary pyrite from disseminated orogenic pyrite in pyritic sedimentary rocks [20,28].

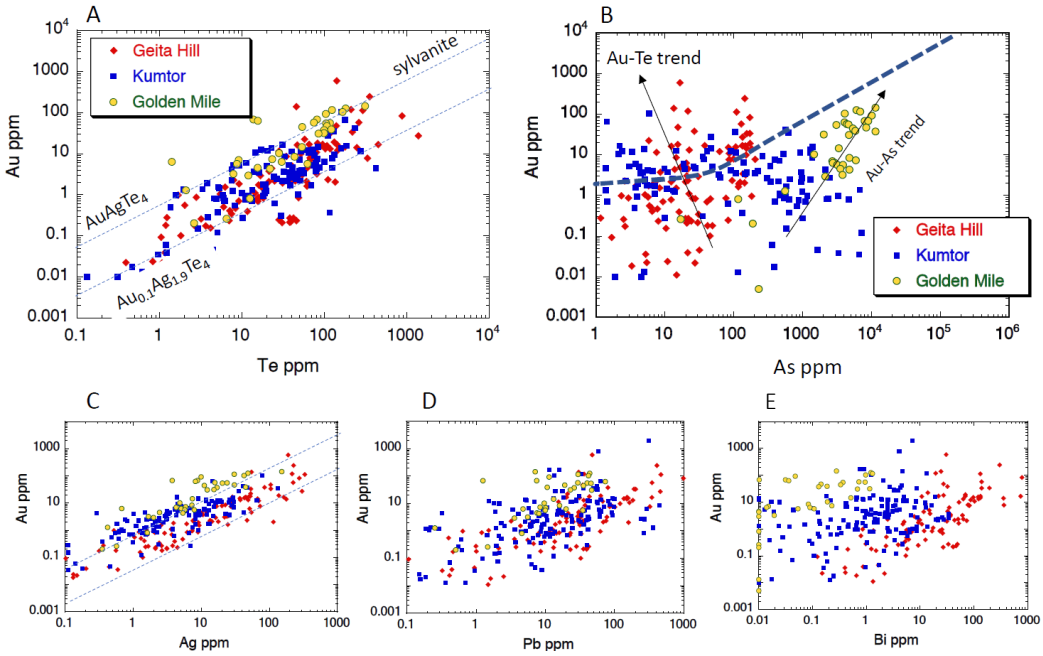

Figure 11. LA-ICPMS data on pyrite for Geita Hill, Kumtor and Golden Mile. The Au-Te and Au-Ag associations suggest Au-Ag tellurides nano- to micro-inclusions in pyrite are a significant host for Au. Golden Mile (Fimiston) pyrite exhibits both an Au-Te and Au-As association. (**A**): Te-Au plot; (**B**): As-Au plot; (**C**): Ag-Au plot; (**D**): Pb-Au plot; (**E**): Bi-Au plot.

Table 2. Mean values of As, Te, Au and Ag in pyrite from the deposits discussed in this study.

Deposit	As ppm	Te ppm	Au ppm	Ag ppm
Carlin Trend	18,050	0.15	158	18.6
Macraes Otago	8480	0.58	112	1.7
Golden Mile	4340	61	35	15.5
Kumtor	633	46.7	26.8	35.1
Mt Olympus	27,292	0.32	26.6	1.1
Geita Hill	53.15	83.9	18.9	40.4
Witwatersrand CLR	1932	8.9	6.51	4.43
Bendigo py halo	5220	1.58	4.13	3.3
Spanish Mountain	5380	2.27	1.76	7.9
Sukhoi Log	3175	1.53	1.61	3.3

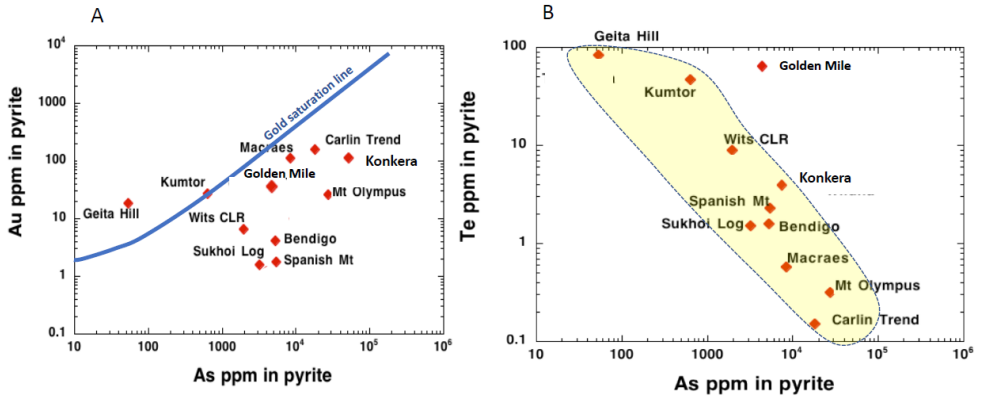

Figure 12. Mean values of Au, As and Te in pyrite from our LA-ICPMS analyses (Table 2) shown on a (**A**) Au-As plot, (**B**) As-Te plot.

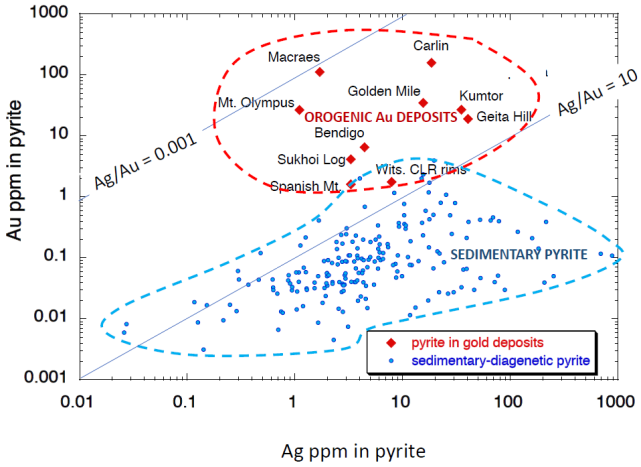

Figure 13. Ag-Au plot showing mean pyrite values for ore deposits compared with data from sedimentary pyrite [28]. The line Ag/Au = 10 roughly divides the two fields.

4.3. Gold-Cobalt-Nickel Relationships in Pyrite

Both Co and Ni occur as stochiometric replacements for Fe in the pyrite structure, and it is common for them to be concentrated in both sedimentary and orogenic pyrites [20,23]. Oscillatory zoning of Ni and Co is particularly common in hydrothermal orogenic pyrites, as well as magmatic-hydrothermal pyrites in IOCG and porphyry Cu-au systems [36]. Most pyrites have a Ni/Co ratio between 0.1 and 10 (Figure 14), although Ni may be considerably enriched, in some cases, especially sedimentary pyrite, compared to cobalt [23]. High temperature hydrothermal pyrites (>~300 °C) tend to be Co-rich [36,49]. The LA-ICPMS maps (Figures 3–11) suggest that Au-As shows greater affinity for Ni-rich orogenic pyrite. Co-rich pyrite is poor in Au and is either pre or post the main gold event (e.g., Spanish Mt., Konkera and Gold Quarry). This feature is clearly demonstrated in Figure 15, where it is shown that orogenic pyrite with Co > 400 ppm rarely carries invisible gold above 3 ppm, whereas pyrite with Co < 100 ppm can carry up to 1150 ppm Au. This negative relationship of Co-Au may be a temperature effect, whereby invisible gold is more common in low-temperature pyrites, than in Co-rich high temperature pyrite. Alternatively, it may relate to the surface charge on the gold transport species and precipitated pyrite, and its capacity to attract gold from the hydrothermal solution [52].

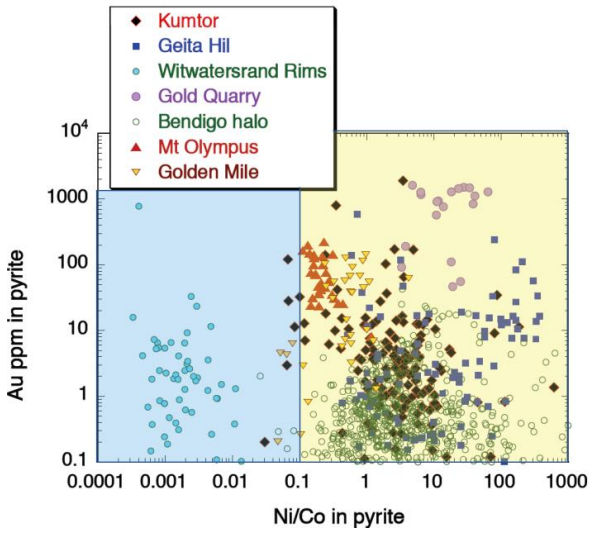

Figure 14. Variation in Au content with Ni/Co ratio in pyrite. Most Au-bearing pyrites have Ni/Co > 0.1. The rims on detrital pyrites in the Witwatersrand CLR are the exception.

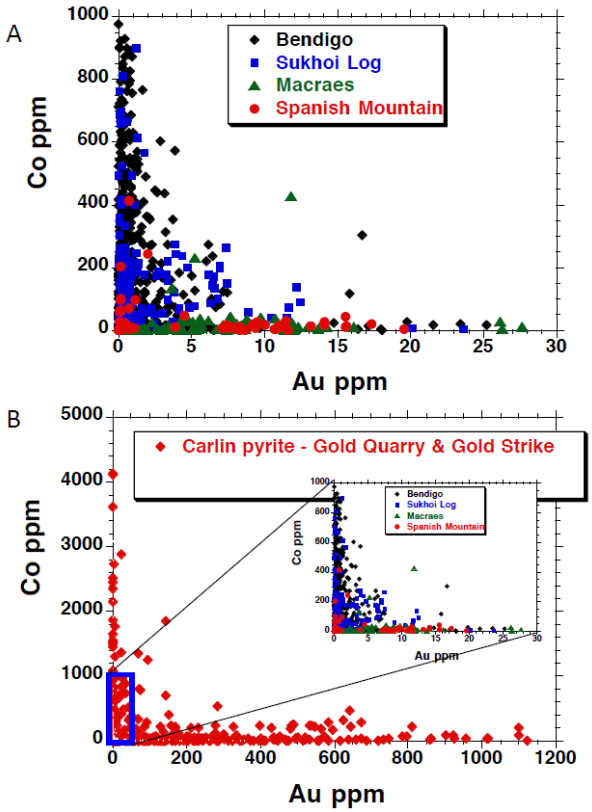

Figure 15. Co-Au relationships in pyrite from selected deposits demonstrates that the highest levels of Au occur in Co-poor pyrite.

Pyrites with a negative surface charge and high electrical conductivity are called p-type and are commonly As-rich pyrite. Pyrites with a positive surface charge are called n-type and are commonly Co-rich and As-poor [53,54]. Our data (Figure 14) suggests that Au is preferentially attracted to the high conductivity negatively charged p-type pyrites (Ni/Co > 0.1) rather than the low-conductivity Co-rich n-type (Ni/Co < 0.1), although Witwatersrand CLR appears to be an exception (Figure 14).

5. Importance of Gold-Rich Rims on Pyrite

Invisible gold-rich rims on arsenian pyrite are best developed in Carlin-type deposits, but we also report them from the Witwatersrand CLR and Bendigo pyrite halo. In Carlin ores, the rims contain hundreds to thousands of ppm invisible gold but no free gold, whereas the rims on detrital pyrites in the CLR have low levels of invisible gold (0.5 to 10 ppm), but micro-inclusions of free gold (Figures 6 and 10). This is probably due to a change in the position of the gold saturation line between the two deposit types (Figure 10B). Gold-rich rims can "turn a sows ear into a silk purse"—in other words a low-grade Au deposit with poor metallurgical characteristics can become a high-grade deposit with improved metallurgical characteristics (e.g., Spanish Mountain compared to Calin). Only deposits of the Au-As association develop Au-rich rims on pyrite, which we assume is because the gold in the hydrothermal fluid is readily attracted to the p-type As-rich pyrite, but not to the n-type Co-rich pyrite. The Au-Te association deposits of Geita Hill, Kumtor, and Macraes do not exhibit Au-rich rims on pyrite. The pyrite in these deposits contain internal nano- to micro-inclusions of free Au and Au-Ag(-Pb-Bi) tellurides.

6. Comments on Transport of Au and As in Orogenic Fluids

Experimental studies support the transport of gold in hydrothermal fluids as complexes with chloride or bisulfide, in particular $AuCl_2^-$, $Au(HS)_2^-$ and $AuHS^0$ ([55] and references therein). However

the very consistent association in orogenic and sediment-hosted deposits of either Au coupled with As or Au coupled with Te suggests the possibility that the gold is transported in some form of soluble complex or colloid of either Au-As-S or Au-Te-S (±Ag-Pb-Bi). This possibility has previously been suggested [56] but no experimental studies have been undertaken to confirm such complex transport.

Another potential form of Au transport in sedimentary basins is by organic-rich (oil-bearing) fluids. This process is given support by recent experimental studies [57] and could explain the unusual chemical composition of the Au-As-Te rims on detrital pyrites (Figure 8) in the Witwatersrand CLR [58]. The mechanism of deposition of gold on pyrite, whether by sulfidation or chemisorption, or by dual precipitation is beyond the scope of this article. Readers are referred to the papers [14,52,53].

7. Conclusions

In this paper, we have attempted to determine the timing and chemical association of Au relative to the growth of pyrite aggregates from successive orogenic fluid events through a combination of textural studies of pyrite, with LA-ICPMS mapping and spot analyses on eleven orogenic deposits. We have showed that gold introduction maybe early orogenic in the core of the pyrite (Geita Hill and Spanish Mt.), late orogenic in the rim (Gold Quarry, Bendigo halo, Witwatersrand CLR) or mid-orogenic within internal pyrite zones (Mt. Olympus, Macraes and Konkera). These eleven deposits form a spectrum, from those where invisible Au is associated with arsenian pyrite to those where the gold occurs in low-arsenic pyrite as micro-inclusions of Au-Ag tellurides (±Pb and Bi). In Gold Quarry (Carlin type) pyrite, the maximum amount of invisible gold per % arsenic is achieved in the rim of the pyrites and is an order of magnitude greater than invisible gold content in pyrites from other Au-As-associated deposits. Kumtor and Geita Hill show the Au-Te association with micro-grains and invisible Au-Ag-tellurides in internal pyrite grain boundaries or fractured pyrite. Golden Mile pyrites exhibit strong correlations of both Au-As and Au-Te. Some deposits (e.g., Witwaterand CLR) have Au-bearing rims on detrital pyrite which carry both As and Te and suggest a significant orogenic hydrothermal event overprinting the reefs. Generally, pyrites with Ni/Co > 0.1 carry the higher levels of invisible Au and As. This may relate to the surface charge on pyrite being dependent on As content and Ni/Co ratio, with the more Ni-As-rich pyrites (n-type) being favourable for gold capture from the hydrothermal fluid compared with the p-type As-poor, Co-rich pyrites.

Author Contributions: Conceptualization, R.R.L. and V.V.M.; methodology R.R.L. and V.V.M.; formal analysis, R.R.L.; investigation, R.R.L. and V.V.M.; resources, R.R.L.; data curation, R.R.L.; writing—original draft preparation, R.R.L.; writing—review and editing, R.R.L. and V.V.M.; project administration, R.R.L.; funding acquisition, R.R.L. All authors have read and agreed to the published version of the manuscript."

Funding: This research was funded by the Australian Research Council, AMIRA International and the Australian Research Council Hub for Transforming the Mining Value Chain, University of Tasmania.

Acknowledgments: Jeff Steadman provided analytical data on pyrite from the Fimiston lodes, Golden Mile, and made useful comments on an early version of the manuscript. This research would not be possible without Leonid Danyushevsky and his team who keep the LA-ICPMS lab at CODES running smoothly. Thanks to the sponsor exploration companies who supported this research and to AMIRA International for coordination of Project P1041.

Conflicts of Interest: The authors declare no conflict of interest.

References

1. Chryssoulis, S.L.; McMullen, J. Mineralogical investigation of gold ores. *Dev. Miner. Process.* **2005**, *15*, 21–71.
2. Chryssoulis, S.; Dunne, R.; Coetzee, A. Diagnostic microbeam technology in gold ore processing. *JOM* **2004**, *56*, 53–57. [CrossRef]
3. Spry, P.G.; Chryssoulis, S.; Ryan, C.G. Process mineralogy of gold: Gold from telluride-bearing ores. *JOM* **2004**, *56*, 60–62. [CrossRef]
4. Reich, M.; Kesler, S.E.; Utsunomiya, S.; Palenik, C.S.; Chryssoulis, S.L.; Ewing, R. Solubility of gold in arsenian pyrite. *Geochem. Cosmochim. Acta* **2005**, *69*, 2781–2796. [CrossRef]

5. Deditius, A.P.; Reich, M.; Kesler, S.E.; Utsunomiya, S.; Chryssoulis, S.L.; Walshe, J.; Ewing, R.C. The coupled geochemistry of Au and As in pyrite from hydrothermal ore deposits. *Geochim. Cosmochim. Acta* **2014**, *140*, 644–670. [CrossRef]
6. Bortnikov, N.S.; Cabri, L.J.; Vikentiev, I.V.; Tagirov, B.R.; Mc Mahon, G.; Bogdanov, Y.A.; Stavrova, O.O. Invisible gold in sulfides from seafloor massive sulfide edifices. *Geol. Ore Depos.* **2003**, *45*, 201–212.
7. Maslennikov, V.V.; Maslennikova, S.P.; Large, R.R.; Danyushevsky, L.V. Study of trace element zonation in vent chimneys from the Silurian Yaman-Kasy volcanic-hosted massive sulfide deposit (Southern Urals, Russia) using laser ablation-inductively coupled plasma mass spectrometry (LA-ICPMS). *Econ. Geol.* **2009**, *104*, 1111–1141. [CrossRef]
8. Vikentyev, I.V. Invisible and microscopic gold in pyrite: methods and new data for massive sulfide ores of the Urals. *Geol. Ore Depos.* **2015**, *57*, 237–265. [CrossRef]
9. Cook, N.J.; Chryssouilis, S.L. Concentrations of invisible gold in the common sulfides. *Can. Mineral.* **1990**, *28*, 1–16.
10. Mumin, A.H.; Fleet, M.E.; Chryssoulis, S.L. Gold mineralisation in As-rich mesothermal gold ores of the Bogosu-Prestea mining district of the Ashanti Gold Belt, Ghana: remobalization of "invisible" gold. *Miner. Depos.* **1994**, *29*, 445–460. [CrossRef]
11. Deditius, A.P.; Utsunomiya, S.; Ewing, R.C.; Kesler, S.E. Nanoscale "liquid" inclusions of As-Fe-S in arsenian pyrite. *Am. Mineral.* **2009**, *94*, 391–394. [CrossRef]
12. Abraitis, P.K.; Pattrick, R.A.D.; Vaughan, D.J. Variations in the compositional, textural and electrical properties of natural pyrite: A review. *Int. J. Miner. Process.* **2004**, *74*, 41–59. [CrossRef]
13. Cline, J.S. Timing of gold and arsenic sulphide mineral deposition at the Getchell Carlin-type gold deposit, north central Nevada. *Econ. Geol.* **2001**, *96*, 75–89. [CrossRef]
14. Kusebauch, C.; Gleeson, S.A.; Oelze, M. Coupled partitioning of Au and As into pyrite controls formation of giant Au deposits. *Sci. Adv.* **2019**, *5*, eaav5891. [CrossRef] [PubMed]
15. Cabri, L.J. Phase relations in the Au-Ag-Te systems and their mineralogical significance. *Econ. Geol.* **1965**, *60*, 1569–1606. [CrossRef]
16. Ciobanu, C.L.; Cook, N.J.; Spry, P.G. Preface-Special Issue: Telluride and selenide minerals in gold deposits-how and why? *Mineral. Petrol.* **2006**, *87*, 163–169. [CrossRef]
17. Cook, N.J.; Ciobanu, C.L.; Spry, P.G.; Voudouris, P. Understanding gold-(silver)-telluride-(selenide) mineral deposits. *Episodes* **2009**, *32*, 249–263. [CrossRef]
18. Zhao, J.; Pring, A. Mineral Transformations in Gold–(Silver) Tellurides in the Presence of Fluids: Nature and Experiment. *Minerals* **2019**, *9*, 167. [CrossRef]
19. Danyushevsky, L.V.; Robinson, P.; Gilbert, S.; Norman, M.; Large, R.R.; Mc-Goldrick, P.; Shelley, J.M. A technique for routine quantitative multi-element analysis of sulphide minerals by laser ablation ICPMS. *Geochem. Explor. Environ. Anal.* **2011**, *11*, 51–60. [CrossRef]
20. Large, R.R.; Danyushevsky, L.; Hollit, C.; Maslennikov, V.; Meffre, S.; Gilbert, S.; Bull, S.; Scott, R.; Emsbo, P.; Thomas, H.; et al. Gold and trace element zonation in pyrite using a laser imaging technique: Implications for the timing of gold in orogenic and Carlin-style sediment-hosted deposits. *Econ. Geol.* **2009**, *104*, 635–668. [CrossRef]
21. Large, R.R.; Meffre, S.; Burnett, R.; Guy, B.; Bull, S.; Gilbert, S.; Goemann, K.; Danyushevsky, L. Evidence for an intrabasinal source and multiple concentration processes in the formation of the Carbon Leader Reef, Witwatersrand Supergroup, South Africa. *Econ. Geol.* **2013**, *108*, 1215–1241. [CrossRef]
22. Longerich, H.P.; Jackson, S.E.; Gunther, D. Laser ablation inductively coupled plasma mass spectrometric transient signal data acquisition and analyte concentration calculation. *J. Anal. At. Spectrom.* **1996**, *11*, 899–904. [CrossRef]
23. Large, R.R.; Maslennikov, V.; Robert, F.; Danyushevsky, L.V.; Chang, Z. Multistage sedimentary and metamorphic origin of pyrite and gold in the giant Sukhoi Log deposit, Lena gold province, Russia. *Econ. Geol.* **2007**, *102*, 1233–1267. [CrossRef]
24. Thomas, H.V.; Large, R.R.; Bull, S.W.; Maslennikov, V.; Berry, R.F.; Fraser, R.; Froud, S.; Moye, R. Pyrite and pyrrhotite textures and composition in sediments, laminated quartz veins, and reefs at Bendigo gold mine, Australia: Insights for ore genesis. *Econ. Geol.* **2011**, *106*, 1–31. [CrossRef]

25. Meffre, S.; Large, R.R.; Steadman, J.A.; Gregory, D.D.; Stepanov, A.S.; Kamenetsky, V.S.; Ehrig, K.; Scott, R.J. Multi-stage enrichment processes for large gold-bearing ore deposits. *Ore Geol. Rev.* **2016**, *76*, 268–279. [CrossRef]
26. Safina, N.P.; Maslennikov, V.V. Sequence of mineral formation in clastic ores of the Saf'yanovka volcanic-hosted copper massive sulfide deposit, the Central Urals. *Geol. Ore Depos.* **2009**, *51*, 633–634. [CrossRef]
27. Panteleyev, A.; Bailey, D.G.; Bloodgood, M.A.; Hancock, K.D. Geology and mineral deposits of the Quesnel River–Horsefly map area, central Quesnel Trough, British Columbia (NTS map sheets 93A/5, 6, 7, 11, 12, 13; 93B/9, 16; 93G/1; 93H/4): BC Ministry of Energy, Mines and Petroleum Resources. *Geol. Surv. Branch Bull.* **1996**, *97*, 156.
28. Gregory, D.D.; Large, R.R.; Halpin, J.A.; Baturina, E.L.; Lyons, T.W.; Wu, S.; Danyushevsky, L.; Sack, P.J.; Chappaz, A.; Maslennikov, V.V.; et al. Trace element content of sedimentary pyrite in black shales. *Econ. Geol.* **2015**, *110*, 1389–1410. [CrossRef]
29. Phillips, G.N.; Groves, D.I.; Martyn, J.E. An epigenetic origin for Archean banded iron-formation-hosted gold deposits. *Econ. Geol.* **1984**, *79*, 162–171. [CrossRef]
30. Arehart, G.B.; Foland, K.A.; Naeser, C.W.; Kesler, S.E. $^{40}Ar/^{39}Ar$, K/Ar, and fission track geochronology of sediment-hosted disseminated gold deposits at Post-Betze, Carlin Trend, northeastern Nevada. *Econ. Geol.* **1993**, *88*, 622–646. [CrossRef]
31. Gopon, P.; Douglas, J.O.; Auger, M.A.; Hansen, L.; Wade, J.; Cline, J.S.; Robb, L.J.; Moody, M.P. A Nanoscale Investigation of Carlin-Type Gold Deposits: An Atom-Scale Elemental and Isotopic Perspective. *Econ. Geol.* **2019**, *114*, 1123–1133. [CrossRef]
32. Law, J.D.; Phillips, G.N. Hydrothermal replacement model for Witwatersrand gold. In *100th Anniversary Volume*; Society of Economic Geologists: Littleton, CO, USA, 2005; pp. 799–812.
33. Tan, Q.; Xia, Y.; Xie, Z.; Wang, Z.; Wei, D.; Zhao, Y.; Yan, J.; Li, S. Two Hydrothermal Events at the Shuiyindong Carlin-Type Gold Deposit in Southwestern China: Insight from Sm–Nd Dating of Fluorite and Calcite. *Minerals* **2019**, *9*, 230. [CrossRef]
34. Frimmel, H.E.; Groves, D.I.; Kirk, J.; Ruiz, J.; Chesley, J.; Minter, W.E. The formation and preservation of the Witwatersrand goldfields, the world's largest gold province. *Econ. Geol.* **2005**, *100*, 769–797.
35. Cox, S.F.; Sun, S.S.; Etheridge, M.A.; Wall, V.J.; Potter, T.F. Structural and geochemical controls on the development of turbidite-hosted gold quartz vein deposits, Wattle Gully Mine, central Victoria, Australia. *Econ. Geol.* **1995**, *90*, 1722–1746. [CrossRef]
36. Steadman, J.A.; Large, R.R.; Meffre, S. Pyrite textures and chemical zoning in magmatic hydrothermal ores. *Minerals* **2020**. (in preparation).
37. Sener, A.K.; Young, C.; Groves, D.I.; Krapez, B.; Fletcher, I.R. Major orogenic gold episode associated with Cordilleran-style tectonics related to the assembly of Paleoproterozoic Australia? *Geology* **2005**, *33*, 225–228. [CrossRef]
38. Fielding, I.O.; Johnson, S.P.; Meffre, S.; Zi, J.W.; Sheppard, S.; Large, R.R.; Rasmussen, B. Linking gold mineralization to regional-scale drivers of mineral systems using in situ U–Pb geochronology and pyrite LA-ICP-MS. *Geosci. Front.* **2018**, *30*, 89–105. [CrossRef]
39. Maclean. *NI 43101 Technical Report on the Konkera Gold Project for Ampella Mining Limitwd*; Ravensgate Mining Industry Consultants: West Perth, Australia, 2014; 165p.
40. Kitto, P.; Shepherd, R.; Rudd, T.; Ouedraogo, S. Konkera gold discovery: Unearthing a new gold province at Batie West in southern Burkina Faso. In Proceedings of the NewGen Gold 2011 Conference, Case Histories of Discovery, Perth, Australia, 12–13 November 2011.
41. Large, R.R. *Pyrite Textures and LA-ICPMS Trace Element Zonation; Defining the Main Gold Event at Konkera Gold Deposit, Burkina Faso*; Consultant report to Ampella; University of Tasmania: Hobart, Australia, 2011; 70p.
42. Craw, D.; Windle, S.J.; Angus, P.V. Gold mineralization without quartz veins in a ductile-brittle shear zone, Macraes Mine, Otago Schist, New Zealand. *Miner. Depos.* **1999**, *34*, 382–394. [CrossRef]
43. Pitcairn, I.K.; Teagle, D.A.; Craw, D.; Olivo, G.R.; Kerrich, R.; Brewer, T.S. Sources of metals and fluids in orogenic gold deposits: Insights from the Otago and Alpine Schists, New Zealand. *Econ. Geol.* **2006**, *101*, 1525–1546. [CrossRef]
44. Henne, A.; Craw, D. Synmetamorphic carbon mobility and graphite enrichment in metaturbidites as a precursor to orogenic gold mineralisation, Otago Schist, New Zealand. *Miner. Depos.* **2012**, *47*, 781–797. [CrossRef]

45. Large, R.; Thomas, H.; Craw, D.; Henne, A.; Henderson, S. Diagenetic pyrite as a source for metals in orogenic gold deposits, Otago Schist, New Zealand. *New Zealand J. Geol. Geophys.* **2012**, *55*, 137–149. [CrossRef]
46. Van Ryt, M.R.; Sanislav, I.V.; Dirks, P.H.; Huizenga, J.M.; Mturi, M.I.; Kolling, S.L. Alteration paragenesis and the timing of mineralised quartz veins at the world-class Geita Hill gold deposit, Geita Greenstone Belt, Tanzania. *Ore Geol. Rev.* **2017**, *91*, 765–779. [CrossRef]
47. Seltmann, R.; Jenchuraeva, R. *Paleozoic Geodynamics and Gold Deposits in the Kyrgyz Tien Shan Excursion Guidebook*; International Geological Correlation Programme: Montreal, QC, Canada, 2001.
48. Yakubchuk, A.S. Gold and base metal metallogeny of the Central Asian orogenic supercollage. *Econ. Geol.* **2005**, *100*, 1035–1068.
49. Huston, D.L.; Sie, S.H.; Suter, G.F.; Cooke, D.C.; Both, R.A. Trace elements in sulfide minerals from eastern Australian volcanic-hosted massive sulfide deposits: Part 1 Proton microprobe analyses of pyrite, chalcopyrite and sphalerite. *Econ. Geol.* **1995**, *90*, 1167–1196. [CrossRef]
50. Pals, D.W.; Spry, P.G. Telluride mineralogy of the low-sulfidation epithermal Emperor gold deposit, Vatukoula, Fiji. *Mineral. Petrol.* **2003**, *79*, 285–307. [CrossRef]
51. Simon, G.; Kesler, S.E.; Chryssoulis, S. Geochemistry and textures of gold-bearing arsenian pyrite, Twin Creeks, Nevada; implications for deposition of gold in Carlin-type deposits. *Econ. Geol.* **1999**, *94*, 405–421. [CrossRef]
52. Luo, S.; Nie, X.; Yang, M.; Fu, Y.; Zeng, P.; Wan, Q. Sorption of Differently Charged Gold Nanoparticles on Synthetic Pyrite. *Minerals* **2018**, *8*, 428. [CrossRef]
53. Pridmore, D.F.; Shuey, R.T. The electrical resistivity of galena, pyrite, and chalcopyrite. *Am. Mineral.* **1976**, *61*, 248–259.
54. Savage, K.S.; Stefan, D.; Lehner, S.W. Impurities and heterogeneity in pyrite: Influences on electrical properties and oxidation products. *Appl. Geochem.* **2008**, *23*, 103–120. [CrossRef]
55. Pokrovski, G.S.; Akinfiev, N.N.; Borisova, A.Y.; Zotov, A.V.; Kouzmanov, K. Gold speciation and transport in geological fluids: insights from experiments and physical-chemical modelling. *Geol. Society Lond. Spec. Publ.* **2014**, *402*, 9–70. [CrossRef]
56. Boyle, R.W. Hydrothermal transport and deposition of gold. *Econ. Geol.* **1969**, *64*, 112–115. [CrossRef]
57. Williams-Jones, A.E.; Migdisov, A.A.; Andrew, C.J. The solubility of gold in crude oil: Implications for ore genesis. In Proceedings of the 9th Biennal SGA Meeting, Millpress, Dublin, Ireland, 20–23 August 2007.
58. Williams-Jones, A.E.; Bowell, R.J.; Migdisov, A.A. Gold in solution. *Elements* **2009**, *5*, 281–287. [CrossRef]